fibers

MDPI

Article

A High-Flexibility Contact Force Sensor Based on the 8-Shaped Wound Polymer Optical Fiber for Human Safety in Human–Robot Collaboration

Yi Liu [1,2], Yaru Zuo [1,2], Xueyao Jiang [1,2], Xuezhu Li [1,2], Weihao Yuan [3,*] and Wenhong Cao [4]

[1] School of Mechanical and Electronic Engineering, Wuhan University of Technology, Wuhan 430070, China; wgdliuyi2001@126.com (Y.L.); zuo_yr2000@163.com (Y.Z.);whutjxy@163.com (X.J.); lixuezhu2856@163.com (X.L.)
[2] Shaoxing Institute for Advanced Research, Wuhan University of Technology, Shaoxing 321000, China
[3] National Key Laboratory of Microwave Photonics, Nanjing University of Aeronautics and Astronautics, Nanjing 211106, China
[4] Zhejiang Rein Hytec Co., Ltd., Shaoxing 321000, China; caownehong@rein.net.cn
* Correspondence: weihao.yuan@nuaa.edu.cn

Abstract: Human–robot collaboration is a new trend in modern manufacturing. Safety, or human protection, is of great significance due to humans and robots sharing the same workshop space. To achieve effective protection, in this paper, a contact force sensor based on an 8-shaped wound polymer optical fiber is proposed. The 8-shaped wound structure can convert the normal contact force to the shrinkage of the 8-shaped optical fiber ring. The macro-bending loss of the optical fiber is used to detect the contact force. Compared with conventional sensors, the proposed scheme has the advantage of high flexibility, low cost, fast response, and high repeatability, which shows great promise in actively alerting users to potential collisions and passively reducing the harm caused to humans.

Keywords: human–robot collaboration; soft sensor; force sensor; optical fiber sensor; polymer optical fiber sensor

check for updates

Academic Editors: Martin J. D. Clift and Andrey Pryamikov

Received: 23 July 2024
Revised: 7 November 2024
Accepted: 14 January 2025
Published: 2 February 2025

Citation: Liu, Y.; Zuo, Y.; Jiang, X.; Li, X.; Yuan, W.; Cao, W. A High-Flexibility Contact Force Sensor Based on the 8-Shaped Wound Polymer Optical Fiber for Human Safety in Human–Robot Collaboration. *Fibers* **2025**, *13*, 15. https://doi.org/10.3390/fib13020015

Copyright: © 2025 by the authors. Licensee MDPI, Basel, Switzerland. This article is an open access article distributed under the terms and conditions of the Creative Commons Attribution (CC BY) license (https://creativecommons.org/licenses/by/4.0/).

1. Introduction

To expand new fields of application as service robots or assistance systems, new trends in human–robot collaboration (HRC) are erasing the boundaries between humans and robots. The safety and protection of humans have become the focus, especially when humans and robots share the same workspace and sometimes even have physical contact with each other. A key technology for safe physical human–robot interaction is the monitoring of contact forces. In 2016, the International Organization of Standardization (ISO) published Technical Specification (TS) 15066, which emphasizes the safety requirements for collaborative industrial robot systems [1], which aims to limit the force transfer from the robot to the human body. To monitor the contact force, many measuring methods were proposed. In the early stage, the robot systems did not attach any extra force sensor and only relied on the joint current monitoring paired with gravity models to calculate the contact forces indirectly. But misjudgments often occur [2]. Ge et al. designed a capacitive and piezoresistive hybrid sensor for long-distance proximity and wide-range force detection [3]. Hua et al. reported a novel modular 3-axis force sensor for a grasping system. Through the calibration model of the modular 3-axis force sensor, a heavy object could be transferred to a human hand in a more compliant manner, without obvious impact [4]. In the field of microsurgery, Kourosh Zareinia et al. presented the development of an instrumented

bipolar forceps used to measure tool–tissue interaction force. It is able to measure and record interaction forces between the forceps tips and brain tissue in real-time, allowing surgeons to achieve the surgical objective effectively while maintaining a safe level of force in the tool–tissue interaction [5]. Yim et al. introduced a multi-functional safety sensor for physical human–robot interaction (pHRI). It enables the sensor to detect the human body and the metal sensitively and distinguish whether an object is a human body. The sensor allows the robot to interact with the operator's body for emergency stop and collision avoidance and even interact with conductive objects [6]. The Motor Learning, Assistive and Rehabilitation Robotics laboratory of the Italian Institute of Technology (IIT) developed an end-effector robotic device, WristBot, for the wrist neurorehabilitation of patients with neurological or orthopedic disabilities. Its limits have been the inability to directly measure forces applied by users and the impossibility to know accurately the end-effector position [7]. To deal with this problem, Pippo et al. introduced a force sensor. In addition, the integration of a linear encoder allowed measuring the instantaneous end-effector position on a non-actuated linear guideway, consequently determining the motor torque value and the force applied by the robot to the user [8]. However, when the human is concentrating on his/her own work, he/she often collides with the robots. The active strategy above will be invalidated. In this situation, a soft contact force sensor as a passive strategy could reduce the hurt further. H. Yang et al. reported a pneumatic soft sensor for a soft gripper [9]. It can detect the variation of air pressure in a rubber chamber to evaluate the contact force. However, the reliability of the sealants in the sensor restricts its application to the large areas of the robot's skin. Cho et al. reported a soft force sensor with a horse shoe shape, which was utilized to measure the contact force and provide a tactile sensation to the user. But the detectable range is too limited [10].

As an emerging technology, optical fiber sensors have attracted increasing attention because of their non-conductivity of electricity, immunity to electromagnetic interference, and their capability for monitoring large areas [11,12]. In 2018, the first prototype of a fingertip force sensor based on fiber Bragg grating (FBG) technology was realized and tested. Using cost functions based on the concept of controllable internal forces and controllable motions, preliminary investigations have identified the one among the three proposed solutions that optimizes grasping and manipulation capabilities [13]. In the field of microsurgery, He Zhang et al. presented a 3-DOF force sensor based on fiber Bragg grating (FBG) sensors for retinal microsurgery, achieving 3-DOF force measurement and temperature compensation [14]. In addition, a sensing system consisting of a curved soft matrix embedding an optical fiber equipped with 16 distributed fiber Bragg gratings (FBGs) has been proposed [15]. The polymer optical fiber (POF) has high flexibility and high sensitivity. It is good for high-flexibility contact force sensors. To further enhance the sensitivity and improve the flexibility of POFs, in this paper, an 8-shaped wound polymer optical fiber sensor packaged by Polydimethylsiloxane (PDMS) is proposed. The sensor has a simple optoelectronic scheme (LED–fiber–photodetector). No complicated spectrum measurement is required. Therefore, it is a low-cost, high-speed, high-flexibility, and high-sensitivity contact force monitoring system. The proposed scheme is a promising technique for ensuring safety in human–robot collaboration.

2. Principle and Fabrication of Sensors

2.1. Structure and Principle of Sensors

The sensor consists of two pillars, a piece of optical fiber, a PDMS package, and a base with a rectangle slot which is shown in Figure 1a. The base is 50 mm long and 30 mm wide. The sensor can be regarded as a polymer-based intelligent composite material. Two pillars with screw threads are fixed on the base. Both have a radius of 2.5 mm. The optical

fiber is wound in 8-shaped rings between the two pillars. All of them are packaged by a PDMS matrix. Because of the rectangular slot between the sensor and the base, the soft PDMS sensor can deform under pressure, as shown in Figure 1c. The pillar is made of Polytetrafluoroethylene (PTFE), which has an elastic modulus higher than that of PDMS by two orders of magnitude. When the PDMS layer is pressed by a force, the pillars can be regarded as rigid cylinders and can keep straight. The composite material between the two pillars can be regarded as a beam fixed at the two ends. When the PDMS moves down, the optical fiber embedded in the PDMS moves synchronously. From the front view of the sensor in Figure 1c, the optical fiber bends from a straight line to a curve (blue line), and thus its length increases a lot. From the top view, as shown in Figure 1d, the two ends of the 8-shaped ring are fixed by two pillars and cannot move. The increasing length of the optical fiber in the front view must result in the shrinkage of the 8-shaped ring in the top view. As shown in Figure 1d, the radius of the 8-shaped ring decreases from R (yellow curve) to r (blue curve) as the force applied on the top surface increases. When light propagates in the optical fiber, the output intensity of light is influenced by the bending loss of the fiber. Thus, the sensor can detect the contact force according to the bending loss of the POF. The 8-shaped structure converts the deformation from the vertical plane to the horizontal plane. Comparing to the traditional micro-bending sensor, the proposed sensor detects the macro-bending loss and can sustain a larger deformation. The excellent flexibility of the proposed sensors can be seen from Figure 1b.

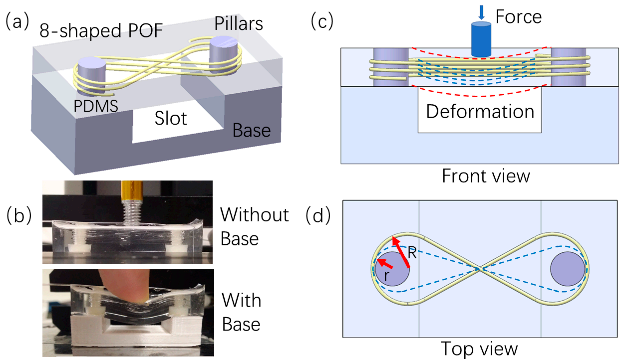


Figure 1. (**a**) The structure of the sensor; (**b**) The photos of the sensors with/without a base; the shrinkage of the 8-shaped ring as the contact force increases; and the principle of the sensor (**c**) from the front view and (**d**) from the top view.

2.2. Model of the Sensor

The sensor structure is made of composite material. The fiber in the sensor is fixed by the pillars, as shown in Figure 2c. Its mechanical model can be regarded as a beam which is fixed at its two ends, as shown in Figure 2a. When a force is put on the beam, the beam bends down. If we ignore the horizontal reaction force, the loading conditions of the beam are shown in Figure 2b.

F_A, M_A, F_B, and M_B represent the reaction forces and moments at support A and support B, respectively. According to the symmetry of the structure, the forces and moments satisfy

$$F_A = F_B, \tag{1}$$

$$M_A = M_B. \tag{2}$$

According to the static equilibrium condition, the reaction forces at the supports can be expressed as

$$F_A = F_B = 0.5F. \tag{3}$$

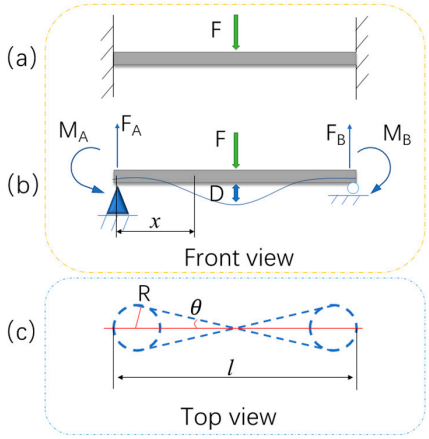


Figure 2. (**a**) A schematic diagram of the mechanical model of the sensor; (**b**) Mechanical model of the sensor when ignoring the horizontal reaction force; (**c**) Geometrical model of the sensor.

In addition, the compatibility condition points out

$$\frac{Fl^2}{16EI} + \frac{M_A l}{3EI} + \frac{M_B l}{6EI} = 0 \tag{4}$$

where E, I, and l represent the elastic modulus, moment inertia, and length of the beam, respectively.

Substituting Equation (2) into (4), one can obtain:

$$M_A = M_B = Fl/8. \tag{5}$$

According to the superposition principle, the deflection curve is

$$D(x) = \begin{cases} \frac{Flx^2}{16EI} - \frac{Fx^3}{12EI} & \left(x < \frac{l}{2}\right) \\ \frac{Fx^3}{12EI} - \frac{3Flx^2}{16EI} + \frac{Fl^2x}{8EI} - \frac{Fl^3}{48EI} & \left(x \geq \frac{l}{2}\right) \end{cases} \tag{6}$$

where x represents the position of a point on the beam, as shown in Figure 2c.

Considering that the radius R of the 8-shaped ring is much smaller than its length l, the influence of the arcs at both ends of the ring on the length of the bent fiber are ignored. The length of the bent fiber L_v can be calculated by

$$L_v = 4\int_0^{l/2} \left(\sqrt{1 + (D'(x))^2}\right) dx. \tag{7}$$

Substituting Equation (6) into (7), the length of the bent fiber L_v can be rewritten as

$$L_v = 4\int_0^{l/2} \left(\sqrt{1 + \left(\frac{F}{4EI}\right)^2 \left(\frac{l}{2}x - x^2\right)^2}\right) dx. \tag{8}$$

The term $\sqrt{1 + \left(\frac{F}{4EI}\right)^2 \left(\frac{l}{2}x - x^2\right)^2}$ is a non-integrable function. However, because of the large elastic modulus value of the material E, the term $\left(\frac{F}{4EI}\right)^2 \left(\frac{l}{2}x - x^2\right)^2$ is much smaller than 1. According to Taylor's theory, Equation (8) can be approximated as

$$\begin{aligned} L_v &\approx 4\int_0^{\frac{l}{2}} \left(1 + \frac{1}{2}\left(\frac{F}{4EI}\right)^2 \left(\frac{l}{2}x - x^2\right)^2\right) dx \\ &= 2l + \frac{1}{7680}\left(\frac{F}{EI}\right)^2 l^5. \end{aligned} \tag{9}$$

For a small force change dF, the length increment dL_v can be written as

$$dL_v = \frac{l^5 F}{3840(EI)^2} dF \tag{10}$$

In Figure 2c, the fiber length of the 8-shaped ring consists of the length of two arcs and two tangent lines which can be expressed as

$$L_h = 4\sqrt{\left(\frac{l}{2} - R\right)^2 - R^2} + 2(2\pi - 2\theta)R \tag{11}$$

where $\theta = \arccos\left(\left(R/(\frac{l}{2} - R)\right)\right)$.

The length decrement of the 8-shaped ring induced by the change in the radius is determined by

$$dL_h = L_h{}'(R)dR \tag{12}$$

where $L_h{}'(R) = 4\arccos\left(\frac{2R}{2R-l}\right) - \frac{4\sqrt{l^2-4Rl}}{(l-2R)}$.

Because of the fiber bending in the vertical plane shown in Figure 2c, the increasing length of fiber results from the shrinkage of the 8-shaped ring in the horizontal plane, which means that

$$dL_h = dL_v. \tag{13}$$

Combining Equations (10), (12), and (13), one can obtain the decrease in the radius as

$$dR = \frac{dL_v}{L_h{}'(R)} = \frac{\frac{l^5 F}{3840(EI)^2} dF}{4\arccos\left(\frac{2R}{2R-l}\right) - \frac{4\sqrt{l^2-4Rl}}{(l-2R)}}. \tag{14}$$

Transition losses of the bent fiber can be evaluated from the overlap integral between optical fields in straight and curved waveguides [16]. The bending loss can be expressed as

$$\text{Loss(dB)} = \int \alpha(R) ds \tag{15}$$

where $\alpha(R)$ is the bending loss per unit length and R is the curvature radius of the fiber.

Marcuse and Marcatili [17,18] analyzed the relationship between the loss and the radius. The macro-bending loss coefficient $\alpha(R)$ satisfies

$$\alpha(R) = \frac{k_1}{\sqrt{R}} e^{-k_2 R} \tag{16}$$

where k_1 and k_2 are constants depending only on the optical properties of the fiber and the wavelength of light. Due to the independence between the curvature radius R and integration variable s in Equation (14), the bending loss can be simplified as

$$\text{Loss} = \frac{k_1}{\sqrt{R}} e^{-k_2 R} \cdot S \tag{17}$$

where S represents the length of the bending fiber.

For a small change in radius dR, the change in loss can be expressed as

$$dLoss = Loss'(R)dR = -k_1 S\left(\frac{1}{2}R^{-1} + k_2\right) R^{-\frac{1}{2}} e^{-k_2 R} dR. \tag{18}$$

Substituting Equation (14) into (18), the sensitivity of the sensor is obtained as shown in Equation (19).

$$\frac{dLoss}{dF} = \frac{-k_1 S\left(\frac{1}{2}R^{-1} + k_2\right)R^{-\frac{1}{2}}e^{-k_2 R}l^5 F}{3840(4\arccos\left(\frac{2R}{2R-l}\right) - \frac{4\sqrt{l^2-4Rl}}{(l-2R)})(EI)^2} \tag{19}$$

Resolving the differential equation, the loss can be obtained as

$$Loss = \frac{-k_1 S\left(\frac{1}{2}R^{-1} + k_2\right)R^{-\frac{1}{2}}e^{-k_2 R}l^5 F^2}{7680(4\arccos\left(\frac{2R}{2R-l}\right) - \frac{4\sqrt{l^2-4Rl}}{(l-2R)})(EI)^2} + C_0 \tag{20}$$

where the constant C_0 represents the initial loss.

The model described by Equation (20) shows that the loss of the sensor is proportional to the term F^2. Only in a small interval of the force can the loss be regarded as a linear function of the force.

2.3. Fabrication and Calibration of Sensors

A simple source–fiber–photodetector system is assembled to calibrate the contact force. The light source is a white LED source (Thorlabs MWWHF2, Thorlabs, Newton, NJ, USA). The fiber is a piece of polymer optical fiber (PMMA) with a diameter of 480 μm and an attenuation of 0.3 dB/m (Dasheng D500, JiangXi DaiShing POF Co., Ltd., Ji'an, China). The matrix of the composite is made of PDMS (Dow Corning SYLGARD 184, Dow Corning, Midland, MI, USA) within a mold. The mix ratio of the base elastomer and the curing agent is 10:1. The curing temperature and time are 60 °C and 120 min, respectively. The photodetector is a power meter with a probe (Thorlabs S142C, Thorlabs, USA) which can receive light with a wavelength range from 350 nm to 1100 nm. The experimental setup is shown in Figure 3. To compare the influence of the base on the sensor, samples with/without a base were manufactured as shown in Figure 1b. The two schemes represent two different installation conditions in practical applications. The force meter is used to load the contact force which is controlled precisely by the computer. In addition, the displacement of the force meter and the power received by the detector are recorded by the computer synchronously.

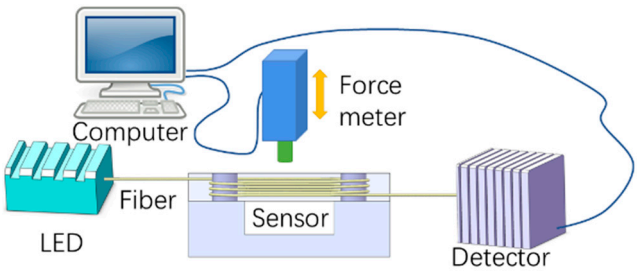


Figure 3. The calibration setup of the contact force.

3. Experiments and Results

3.1. Sensitivity and Hysteresis

A loading/unloading experiment is implemented to test the sensitivity and hysteresis. Figure 4 shows the results of the sensor without the base. The black and blue curves represent the displacement and the power change as the contact force changes, respectively. When the probe of the force meter moves down, both the displacement and the force increase; however, the power decreases. The displacement and the power change almost

linearly as the force increases. The sensitivity of power to the force is −1.82 dBm/N. For a power meter with a resolution of 0.001 dBm, the sensor can theoretically distinguish a minimal force change of 0.55 mN. The sensitivity of displacement to the force is 0.105 mm/N, which is determined by the elastic modulus of PDMS. In the experiment, both the power curve and the displacement curve show a slight hysteresis. It is caused by the stress relaxation of polymer material. In the loading and unloading process, the material undergoes different relaxation processes. This phenomenon will cause measurement errors. From the experimental data, we can calculate that the maximum error is no more than 0.2 N and the maximum error occurs when the force is about 3 N.

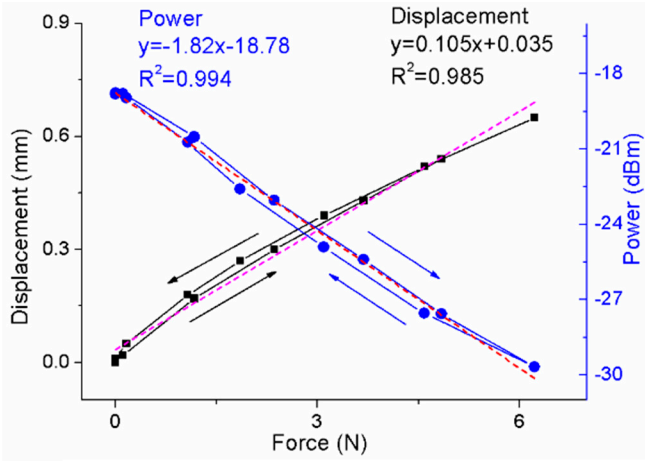


Figure 4. The displacement and the power of the sensor without the base change as the contact force changes in a loading/unloading test.

Figure 5 shows the responses of the sensor with the base. The power response and displacement response also change approximately linearly as the force increases. However, the hysteresis phenomenon becomes strong. It may be caused by the large deformation of the PDMS. In the second experiment, the displacement of the sensor is two times as large as that of the first experiment. The sensitivity of power to the force is −2.16 dBm/N, which is higher than that of the sensor without the base. The sensitivity of displacement to the force is 0.257 mm/N, which shows a lower rigidity than that of the sensor without the base. The low-rigidity sensor is good for reducing the impact force and protecting the human from injury in the human–robot collaboration. In addition, the sensor with the base has a higher sensitivity than that without the base.

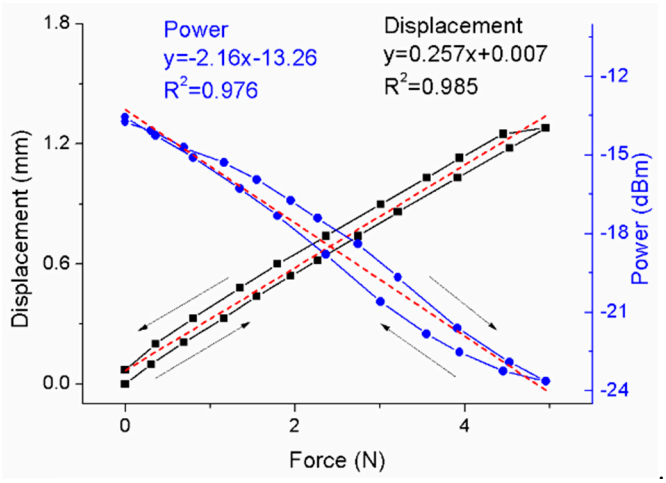


Figure 5. The displacement and the power of the sensor with the base change as the contact force changes in a loading/unloading test.

3.2. Response Rate

The response rate of the sensor is another important characteristic for the human–robot collaboration. Figure 6 shows the response cycle of the sensor in the time domain. The falling edge and rising edge show that the response time and recovery time of the sensor are 0.4 s and 0.3 s, respectively. Considering the slow mechanical motion of the force-loading probe, the real response time and recovery time should be shorter than those of the experimental results.

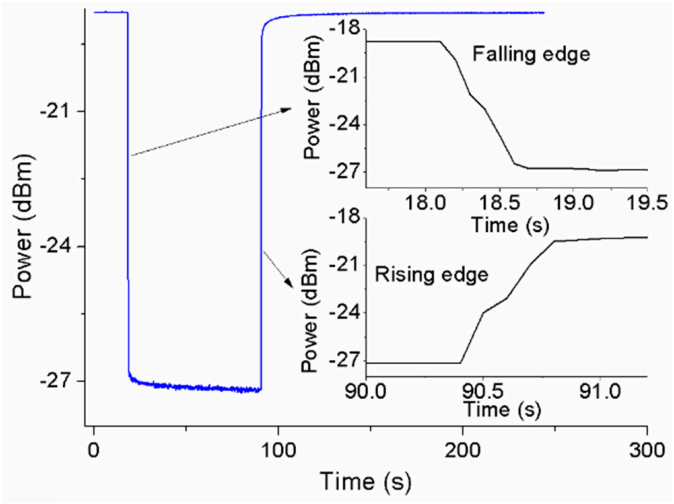


Figure 6. The response of the sensor in the time domain.

3.3. Repeatability

In industrial applications, repeatability is the most important characteristic. Force cycling tests are implemented. The experiment was conducted with a cycle of 200 s, and lasted for 12 h, with the number of cycles exceeding 216. The results of the two samples are shown in Figure 7. Both sensors with the base and without the base show high repeatability. In tens of cycles, the baseline and response line remain straight. The high repeatability benefits from the simple LED–fiber–photodetector structure and composite material package.

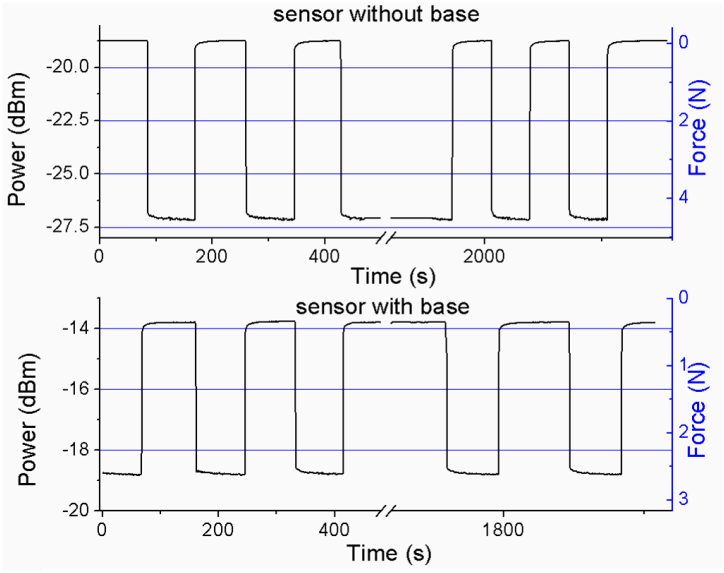


Figure 7. The repeatability of the sensor with the base and the sensor without the base.

4. Discussion

4.1. Simulation Analysis

The parameters of the 8-shaped ring in our experiments are shown in Table 1.

Table 1. Parameters of the 8-shaped ring.

Symbol	Quantity	Value
l	Length of 8-shaped ring	45 mm
R	Initial radius of the 8-shaped ring	2.5 mm
E	Elastic modulus of PDMS	5 Mpa
I	Moment inertia	0.060 cm^4
k_1	Parameter of fiber	0.8356 dB $mm^{-1/2}$
k_2	Parameter of fiber	0.9889 mm^{-1}
n	Turns of the 8-shaped ring	5

The parameters k_1 and k_2 are obtained from Equation (16), according to the losses of PMMA POF, which are reported in Ref. [19]. The losses for the step index-POF with a diameter of 500 μm are 0.7 and 0.2 dB/turn for 2.5 and 4 mm bend radii, respectively.

With these parameters, a simulation was implemented. Figure 8a shows that the displacement and the loss change inversely as the force increases, as what has been measured by the experiments shown in Figure 4. The displacement curve (black curve) is linear to the force. However, the loss (blue curve) is a quadratic function of the force. The loss curve can be approximated by a straight line within a small variation range of the force. This explains why the sensor for large deformation measurement will show a nonlinear sensitivity, as shown in Figure 5.

Figure 8b shows the loss changes as the force changes for different section moment inertia values I. The loss increases as the section moment inertia decreases. It is caused by a reduction in the rigidness. The weak rigidness section results in a large deformation and loss. Therefore, reducing the section moment inertia could be used to increase the sensitivity of the sensor and reduce the harm caused during human–robot collisions. Figure 8c shows the influence of the length of the 8-shaped ring on the loss. For a constant force, the loss increases as the length increases. When $l < 80$ mm, the loss changes a little. However, the loss increases rapidly when the length is longer than 80 mm. For the different forces, the longer the length of the ring is, the larger the difference of the loss between two different forces. In other words, the sensitivity will increase as the length of the 8-shaped ring increases.

4.2. Comparison with Other Force Sensors

From the comparison of the sensors listed in Table 2, it can be seen that our sensor has a simpler structure and relatively higher sensitivity. Furthermore, our sensor can simultaneously measure both force and displacement, which is of great significance for its application in collision prevention during human–machine interaction. By comparing with other sensors, we have also identified that we should develop in the direction of three-dimensional force measurement.

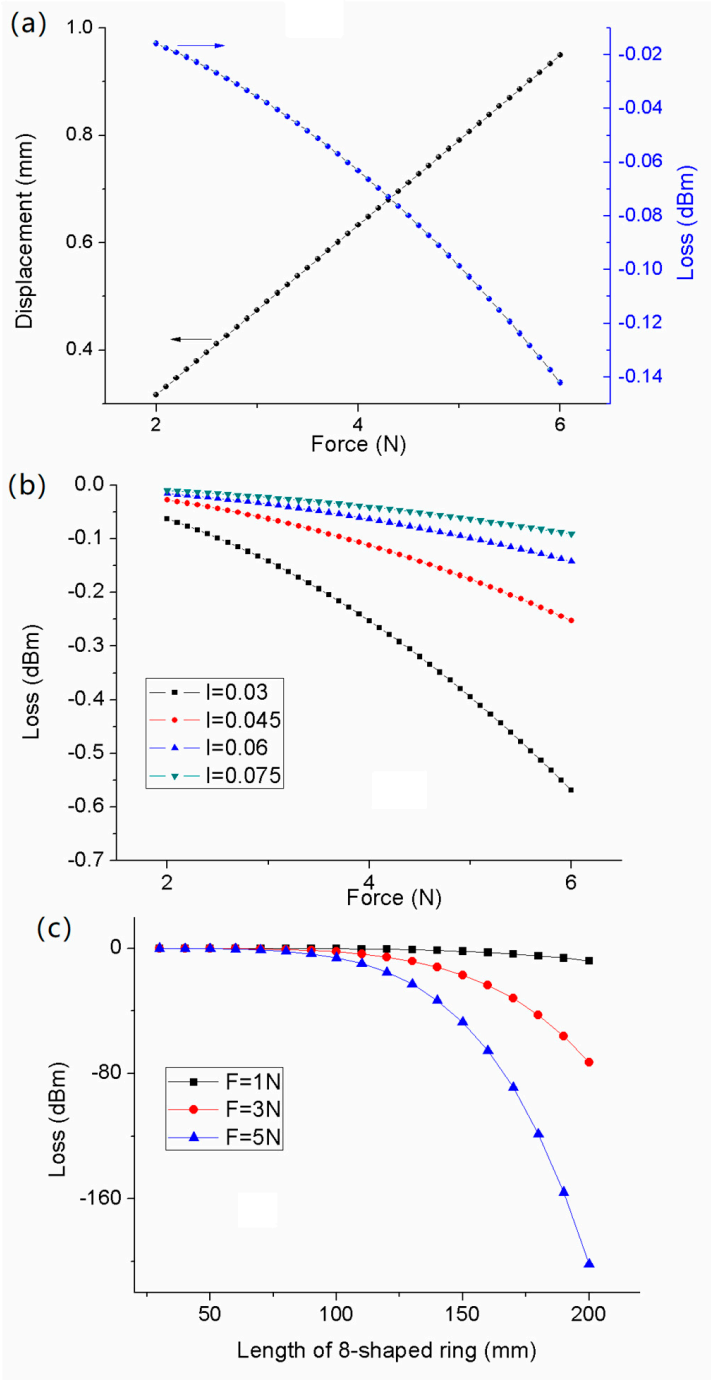


Figure 8. (**a**) The displacement and the loss change as the force increases; (**b**) The loss changes as the force changes for different section moment inertia values *I*; (**c**) The influence of the length of the 8-shaped ring on the loss.

Table 2. Comparison of force sensors in human–robot interactions.

Description	Sensing DOF	Resolution	Used Sensors
Ge et al. [3]	2	0.65 mm for object proximity 17.73 N for contact force	Capacitive and piezoresistive hybrid sensor
Hua et al. [4]	3	0.2 N	Modular 3-axis force sensor
Zareinia et al. [5]	2	0.31 N	Two sets of strain gauges
Yang et al. [9]	3	0.05 N	Pneumatic soft sensor
He Zhang et al. [14]	3	0.122 mN for X/Y 1.808 mN for z	3 fibers 4 FBGs
This work	2	0.55 mN	8-shaped fiber

5. Conclusions

Human–robot collaboration is a new trend in modern manufacturing. To increase safety and protect the human, a soft force sensor as a passive strategy was proposed to reduce further harm to the human. For traditional force sensors, there is a trade-off between the flexibility and the sensitivity of the sensor. A soft package could weaken the external action to sensitive points and reduce the sensitivity of the sensors. In this paper, an 8-shaped wound polymer optical fiber sensor packaged by Polydimethylsiloxane (PDMS) was proposed to obtain high flexibility and sensitivity simultaneously. The sensor consists of a simple LED–fiber–photodetector system. Since no complicated spectrum measurement is required, the proposed scheme is a low-cost, high-speed, high-flexibility, and high-sensitivity contact force monitoring system. In the experiments, the prototype of the sensor shows it can monitor the force and the displacement on its surface simultaneously. The response time and recovery time of the sensor are 0.4 s and 0.3 s, respectively. To clarify the principle of the sensor, a model was established. The simulation results show that the optimization of the parameters of the sensor, such as the section moment inertia and the length of the 8-shaped ring, could improve the properties of the sensor further. Because of its high flexibility, low cost, fast response, and high repeatability, the contact force sensor based on the 8-shaped wound polymer optical fiber shows great promise in actively alerting users to potential collisions and passively reducing the harm caused to humans in the industrial robot field.

Author Contributions: Conceptualization, W.Y. and Y.L.; methodology, W.C. and Y.L.; software, W.Y. and Y.L.; validation, Y.L., W.Y. and W.C.; formal analysis, X.J.; investigation, Y.L.; resources, Y.L.; data curation, Y.L.; writing—original draft preparation, Y.L.; writing—review and editing, Y.Z.; visualization, Y.L.; supervision, W.Y. and Y.L.; project administration, X.L.; funding acquisition, Y.L. All authors have read and agreed to the published version of the manuscript.

Funding: This research was funded by Shaoxing Science and Technology Plan Project grant number 2023B41011.

Data Availability Statement: The original contributions presented in this study are included in the article. Further inquiries can be directed to the corresponding author.

Conflicts of Interest: Author Wenhong Cao was employed by the company Zhejiang Rein Hytec Co., Ltd. The remaining authors declare that the research was conducted in the absence of any commercial or financial relationships that could be construed as a potential conflict of interest.

References

1. *ISO/TS 15066*; Robots and Robotic Devices—Collaborative Robots. ISO: Geneva, Switzerland, 2016.
2. Marvel, J.A. Sensors for safe, collaborative robots in smart manufacturing. In Proceedings of the 2017 IEEE Sensors, Glasgow, UK, 29 October–1 November 2017; Volume 2017, pp. 1–3.
3. Ge, C.; Wang, Z.; Liu, Z.; Wu, T.; Wang, S.; Ren, X.; Chen, D.; Zhao, J.; Hu, P.; Zhang, J. A Capacitive and Piezoresistive Hybrid Sensor for Long-Distance Proximity and Wide-Range Force Detection in Human-Robot Collaboration. *Adv. Intell. Syst.* **2022**, *4*, 2100213. [CrossRef]
4. Hua, H.; Liao, Z.; Liu, Y.; Wu, X.; Zhao, J.; Song, J. Compliant human-robot object transfer based on modular 3-axis force sensor for collaborative manufacturing. *ISA Trans.* **2023**, *141*, 482–495. [CrossRef] [PubMed]
5. Zareinia, K.; Maddahi, Y.; Gan, L.S.; Ghasemloonia, A.; Lama, S.; Sugiyama, T.; Yang, F.W.; Sutherland, G.R. A Force-sensing Bipolar Forceps to Quantify Tool-tissue Interaction Forces in Microsurgery. *IEEE/ASME Trans. Mechatron.* **2016**, *21*, 2365–2377. [CrossRef]
6. Yim, H.; Kang, H.; Moon, S.; Kim, Y.; Nguyenb, T.D.; Choi, H.R. Multi-functional safety sensor coupling capacitive and inductive measurement for physical Human–Robot Interaction. *Sens. Actuators A Phys.* **2023**, *354*, 114285. [CrossRef]
7. Iandolo, R.; Marini, F.; Semprini, M.; Laffranchi, M.; Mugnosso, M.; Cherif, A.; De Michieli, L.; Chiappalone, M.; Zenzeri, J. Perspectives and Challenges in Robotic Neurorehabilitation. *Appl. Sci.* **2019**, *9*, 3183. [CrossRef]

8. Pippo, L.; Albanese, G.A.; Zenzeri, J.; Torazza, D.; Berselli, G. Understanding human-robot interaction forces: A new mechanical solution. *Int. J. Interact. Des. Manuf.* **2024**, *18*, 4765–4774. [CrossRef]
9. Yang, H.; Chen, Y.; Sun, Y.; Hao, L. A novel pneumatic soft sensor for measuring contact force and curvature of a soft gripper. *Sens. Actuators A Phys.* **2017**, *266*, 318–327. [CrossRef]
10. Cho, H.; Lee, H.; Kim, Y.; Kim, J. Design of an Optical Soft Sensor for Measuring Fingertip Force and Contact Recognition. *Int. J. Control Autom. Syst.* **2017**, *15*, 16–24. [CrossRef]
11. Liu, Y.; Zhang, J. Model study of the influence of ambient temperature and installation types on surface temperature measurement by using a fiber bragg grating sensor. *Sensors* **2016**, *16*, 975. [CrossRef] [PubMed]
12. Liu, M.; Zhang, E.; Zhou, Z.; Tan, Y.; Liu, Y. Measurement of temperature field for the spindle of machine tool based on optical fiber bragg grating sensors. *Adv. Mech. Eng.* **2013**, *5*, 940626. [CrossRef]
13. Selvaggio, M.; Fontanelli, G.A.; Marrazzo, V.R.; Bracale, U.; Irace, A.; Breglio, G.; Villani, L.; Siciliano, B.; Ficuciello, F. The MUSHA underactuated hand for robot-aided minimally invasive surgery. *Int. J. Med. Robot. Comput. Assist. Surg.* **2019**, *15*, e1981. [CrossRef] [PubMed]
14. Zhang, H.; Yi, H.; Fan, Z.; Pang, L.; Bai, M.; Wang, C.; Zhao, J. An FBG-Based 3-DOF Force Sensor With Simplified Structure for Retinal Microsurgery. *IEEE Sens. J.* **2022**, *22*, 14911–14920. [CrossRef]
15. D'Abbraccio, J.; Aliperta, A.; Oddo, C.M.; Zaltieri, M.; Palermo, E.; Massari, L.; Terruso, G.; Sinibaldi, E.; Kowalczyk, M.; Schena, E. Design and Development of Large-Area FBG-Based Sensing Skin for Collaborative Robotics. In Proceedings of the 2019 II Workshop on Metrology for Industry 4.0 and IoT, Naples, Italy, 4–6 June 2019.
16. Mustieles, F.J.; Ballesteros, E.; Baquero, P. Theoretical S-Bend Profile for Optimization of Optical Wwaveguide Radiation Losses. *IEEE Photonics Technol. Lett.* **1993**, *5*, 551–553. [CrossRef]
17. Marcuse, D. Bending losses of the asymmetric slab waveguide. *Bell Syst. Tech. J.* **1971**, *50*, 2551–2563. [CrossRef]
18. Martacilli, E.A.J. Bends in optical dielectric guides. *Bell Syst. Tech. J.* **1969**, *48*, 2103–2132.
19. Argyros, A.; Lwin, R.; Large, M.C.J. Bend loss in highly multimode fibres. *Opt. Express* **2008**, *16*, 18590–18598. [CrossRef] [PubMed]

Disclaimer/Publisher's Note: The statements, opinions and data contained in all publications are solely those of the individual author(s) and contributor(s) and not of MDPI and/or the editor(s). MDPI and/or the editor(s) disclaim responsibility for any injury to people or property resulting from any ideas, methods, instructions or products referred to in the content.